Journal of Wind Engineering & Industrial Aerodynamics 275 (2026) 106513

Contents lists available at ScienceDirect

Journal of Wind Engineering & Industrial Aerodynamics

journal homepage: www.elsevier.com/locate/jweia

A novel combined experimental and numerical methodology for aerodynamic characterisation of porous media

Marcello Catania [a,*], Filippo Giacomoni [a], Giulia Pomaranzi [a], Paolo Schito [a], Alberto Zasso [a], Claudio Somaschini [a], Luca Patruno [b]

[a] Department of Mechanical Engineering, Politecnico di Milano, Milano, Italy
[b] DICAM, University of Bologna, Bologna, Italy

ARTICLE INFO

Keywords:
Perforated plates
Porous screens
Aerodynamic drag
Wind tunnel testing
Computational fluid dynamics (CFD)
Static-pressure correction
Periodic simulations
Façade aerodynamics

ABSTRACT

This study examines the aerodynamic behaviour of thin perforated plates through a combined experimental and numerical methodology integrating wind-tunnel measurements, fully resolved CFD of the test section, and computationally efficient periodic "modulus" simulations. The objective is to provide reliable and transferable drag coefficients for porous plates employed in façade engineering and flow-control applications.

The three standard approaches for estimating aerodynamic drag (force balance, total-pressure drop, and static-pressure difference across the plate) are systematically compared under imposed flow-rate conditions. Although often treated as equivalent, the methods yield non-coincident results. High-resolution CFD demonstrates that the static-pressure field on the windward face of the plate is intrinsically non-uniform, leading to a systematic overestimation of drag when pointwise static-pressure measurements are used. This motivates the introduction of a physically based correction factor, $\gamma \approx 5\%$, which is experimentally validated and enables static-pressure estimates to be aligned with force-balance data.

Once validated, simulations in cyclic "modulus" configuration (where only the smallest repeating unit of the perforated plate is simulated) accurately reproduce the global aerodynamic response of the plates at a greatly reduced computational cost, enabling extensive parametric analyses. Results show that porosity is the dominant parameter governing drag, whereas the hole pattern mainly affects local flow structures with limited influence on the integrated force.

1. Introduction

Porous elements are widely employed in wind engineering for a variety of purposes, including traffic or pedestrian barriers, windbreaks, and architectural envelopes allowing partial light transmission. More recently, porous panels have also been adopted as cladding elements for building façades, with installation contexts ranging from single-layer envelopes (e.g. parking structures (Kemper and Feldmann, 2019)) to multi-layer systems such as permeable double-skin façades (Pomaranzi et al., 2019, 2021a; Catania et al., 2024b).

The wind interaction with porous elements strongly depends on their installation context. In real applications, porous panels are not subjected to a prescribed uniform approach flow; rather, their loading conditions is imposed by the surrounding building- or bridge-scale flow field, which is shaped by separation, corner vortices, and other highly three-dimensional effects. In addition, intrinsic geometric and flow parameters, including porosity, hole pattern, thickness, and incoming wind angle (Lo et al., 2020; Skvorc and Kozmar, 2023), play a significant role. These combined dependencies make the wind–structure interaction highly configuration-specific, and a general predictive framework is still lacking (Giachetti et al., 2025). Furthermore, the characteristic length scales associated with the local geometry of porous panels are typically one or more orders of magnitude smaller than those associated with the installation context. This scale separation further complicates the problem and poses challenges for both experimental and numerical modelling.

According to approaches currently adopted in the literature, the multiscale nature of the problem is addressed by explicitly modelling the larger scales associated with the installation context, while representing the porous element through a homogenised or equivalent formulation. In wind-tunnel (WT) testing with scaled models, this is typically achieved by employing an equivalent porous layer designed to reproduce the same pressure drop as the full-scale panel (Allori

* Corresponding author.
E-mail addresses: marcello.catania@polimi.it (M. Catania), filippo.giacomoni@polimi.it (F. Giacomoni), giulia.pomaranzi@polimi.it (G. Pomaranzi), paolo.schito@polimi.it (P. Schito), alberto.zasso@polimi.it (A. Zasso), claudio.somaschini@polimi.it (C. Somaschini), luca.patruno@unibo.it (L. Patruno).

https://doi.org/10.1016/j.jweia.2026.106513
Received 9 March 2026; Received in revised form 24 April 2026; Accepted 18 May 2026
Available online 2 June 2026

et al., 2013; Pomaranzi et al., 2019; Tominaga and Shirzadi, 2022). In computational fluid dynamics (CFD), homogenised models based on empirical or semi-empirical formulations (e.g., Darcy–Forchheimer-type laws (Pomaranzi et al., 2021b; Feichtner et al., 2021; Marykovskiy et al., 2024) or porous-jump conditions (Xu et al., 2020, 2023; Tominaga and Shirzadi, 2022)) are commonly adopted instead of explicitly resolving the small openings of the porous structure. Those approaches have proven their effectiveness even when tested in complex-flow conditions, both as stand-alone elements describing wake shape and evolution (Catania et al., 2024a) and with the porous layer coupled with an underlined solid structure, by capturing both local and global aerodynamic effects (Catania et al., 2026). In all cases, the reliability of building-scale predictions critically depends on how the equivalent aerodynamic parameters of the porous element are identified.

A central question, therefore, arises: how should porous elements be aerodynamically characterised in order to achieve such equivalence? Which experimental or numerical methodologies can be reliably employed, and what is their level of accuracy and transferability? Different characterisation approaches rely on distinct assumptions, boundary conditions, and measurable quantities (e.g., total-pressure drop, static-pressure difference), which are not necessarily equivalent. A systematic comparison of currently available characterisation strategies is still missing, but is required to assess their consistency and to clarify the limits of commonly used formulations, particularly when extrapolated toward more complex installation contexts.

To address these methodological challenges, the present study focuses on the canonical case of an isolated perforated plate under uniform flow. Rather than reproducing the full building–porous element interaction, this setup provides a controlled reference framework to directly compare experimental and numerical characterisation methods. Thin perforated plates represent the most reproducible porous geometry, allowing the intrinsic aerodynamic response of the medium to be isolated from building-induced pressure gradients, and are thus considered for the investigation.

The objectives of this study are to: (i) compare different experimental and numerical approaches for the aerodynamic characterisation of perforated plates; (ii) document the aerodynamic behaviour of isolated plates as a benchmark for comparison with existing literature; and (iii) provide practical guidelines for characterisation strategies, discussing how these results serve as input for building-scale wind tunnel tests and homogenised CFD models.

The following section reviews the literature on the aerodynamic characterisation of porous elements, focusing on perforated plates as the simplest representative case for wind engineering applications, and expands on the open questions addressed in this work.

1.1. Literature review

Porous elements, including nets, meshes, windbreaks, and perforated plates, are widely used in wind engineering to modify air flow, reduce loads, or control ventilation. Their aerodynamic behaviour is commonly described through the normal force coefficient, also known as drag coefficient:

$$C_n = \frac{F_n}{0.5\rho U^2 A}, \tag{1}$$

with A the frontal area exposed to a flow of density ρ and velocity U. At non-zero wind angles, a tangential component F_t may arise, with an associated lift coefficient.

$$C_t = \frac{F_t}{0.5\rho U^2 A}. \tag{2}$$

For thin perforated plates, however, the aerodynamic response is dominated by the normal component.

To compare porous and solid panels, many studies adopt the reduction factor

$$K_p = \frac{C_{n,\text{porous}}}{C_{n,\text{solid}}}. \tag{3}$$

A complementary and widely used measure of the aerodynamic influence of the screen is the loss coefficient:

$$K = \frac{\Delta p_t}{0.5\rho U^2}, \tag{4}$$

where Δp_t is the total-pressure jump imposed by the panel and quantifies its overall effect on the flow field.

Porosity β is defined as the ratio between the open area A_v and the frontal area A ($\beta = A_v/A$) and it is typically the primary geometric parameter used to describe the medium. Yet, the size and shape of the openings also play a role through the hydraulic diameter

$$D_H = \frac{4A_H}{P}, \tag{5}$$

with P the perimeter of an individual hole and A_H its area. This characteristic length defines the hole-scale Reynolds number,

$$Re_H = \frac{\rho U D_H}{\mu}, \tag{6}$$

which is used to assess scale effects and ensure the validity of aerodynamic comparisons.

Over the years, various correlations have been proposed to relate K and K_p to porosity and other geometric parameters. A non-exhaustive summary of the most commonly used expressions is reported in Table 1. Classical works on fences and signboards often adopt a generic form

$$K_p = 1 - \beta^n, \tag{7}$$

with $1 \le n \le 2$ (Raju et al., 1988; Letchford, 2001; Guan et al., 2003). Shen et al. (2025) demonstrated that the exponent n depends strongly on the experimental configuration: for an isolated panel, they found $n = 1.66$, while in the presence of a surrounding frame, they obtained $n = 1.26$, highlighting the role of edge effects and three-dimensional flow features. Castellano and Starace (2025) reported yet another behaviour for agro-textile nets, showing a weaker attenuation of aerodynamic forces than predicted by the classical laws (Eq. (7)). These discrepancies confirm that porosity alone is not a sufficient descriptor and that empirical laws are not directly transferable among different screen technologies.

One of the most systematic attempts to quantify the influence of geometric and flow parameters is the experimental campaign by Allori et al. (2013). They tested a wide range of perforated plates with controlled variation of porosity, hole shape, hydraulic diameter, plate thickness, and flow velocity. Their results indicate that, for matched porosity and thickness, the shape of the hole has a negligible influence on the aerodynamic response. Conversely, the ratio between plate thickness and hydraulic diameter, t/D_H, is a dominant parameter: thicker plates exhibit lower pressure drops due to internal channel-like flow within the openings. Moreover, the authors showed that both the drag coefficient C_n and the loss coefficient K become Reynolds-independent for $Re_H > 3000$, supporting the feasibility of simplified wind-tunnel setups operating at moderate flow speeds. A limitation of their study is that only normal flow incidence was considered, leaving open the behaviour under skew winds, which is critical in façade applications.

Wind-angle effects have been investigated less extensively. The classical cosine-squared relation,

$$K(\alpha, \beta) = K(\beta)\cos^2\alpha, \tag{8}$$

introduced by Laws and Livesey (1978) and later used by Richards and Robinson (1999), suggests a purely geometric projection effect. This reduction function is widely accepted, although few exceptions could be find in the literature. Recent CFD studies by Guo et al. (2012) criticise this simple trend. Using pore-resolved simulations, the authors found that the loss coefficient remains roughly constant up to $\alpha \approx 30°$ but then increases significantly, reaching values up to 30% higher at $\alpha = 60°$. These discrepancies originate in part from different definitions of the reference velocity (magnitude versus normal component) and

Table 1
Selected correlations for loss and reduction coefficients of porous elements.

Quantity	Expression	Reference
Reduction factor	$K_p = 1 - \beta^n,\ 1 \le n \le 2$	Raju et al. (1988), Letchford (2001), Guan et al. (2003)
Reduction factor (isolated panel)	$K_p = 1 - \beta^{1.66}$	Shen et al. (2025)
Reduction factor (with frame)	$K_p = 1 - \beta^{1.26}$	Shen et al. (2025)
Reduction factor (agro-nets)	$K_p = 2e^{-0.4\beta}$	Castellano and Starace (2025)
Loss coefficient (agro-nets)	$K = \frac{1-\beta^2}{\beta^2}$	Castellano and Starace (2025)
Loss coefficient (perforated plates)	$K = \frac{(\alpha_1\beta + 2)(\beta - 1)}{\beta^2(\alpha_2 - 1)}$	Xu et al. (2020)

in part from three-dimensional flow features that are not captured by simple projection arguments. The lack of standardisation in both definitions and setups complicates the comparison of different datasets and underlines the need for a more systematic methodology.

In parallel to experimental efforts, several numerical studies have attempted to characterise porous screens using CFD. Explicit modelling of each hole provides insight into pressure-drop mechanisms and confirms the dependence of K on thickness and hydraulic diameter (Guo et al., 2012; Azizi, 2019). Yet, such simulations are computationally expensive and not applicable to façade-scale problems. To overcome these limitations, homogenised models have been introduced. Xu et al. (2020) used large-eddy simulations to derive a refined expression for the loss coefficient (see Table 1), with empirically calibrated constants that match well the experiments of Allori et al. (2013). This approach was extended by Xu et al. (2023), who proposed a pressure–velocity jump (PVJ) model: a zero-thickness interface where both pressure and tangential velocity undergo discontinuities. Their work demonstrates improved accuracy for oblique winds but still requires calibration through experiments or high-fidelity simulations for each screen geometry and tends to underpredict forces when complex flow features such as vena contraction and separation bubbles occur.

For more complex porous screen geometries, such as louvres or expanded meshes, modelling approaches capable of representing flow deflections and induced forces on the screen (beyond drag alone) are required, as shown by Marykovskiy et al. (2024). In their work, the modelling approach is based on the Darcy–Forchheimer model, in which the porous medium is represented by a 3×3 tensor that relates the local velocity vector to the distributed momentum sinks in the Navier–Stokes equations. This formulation naturally couples normal and tangential directions and allows for the representation of lift-like forces. In fact, when porosity is inherently two- or three-dimensional, the flow is strongly deflected within the porous volume. As a consequence, the tangential force component, expressed by C_t, can become comparable in magnitude to the normal component C_n, especially at oblique angles of attack and for large t/D_H ratios. Accurate measurements of both drag and lift as functions of α and t/D_H are therefore crucial for calibrating the Darcy–Forchheimer tensor and for reliably predicting the aerodynamic response of 2D/3D porous façades.

1.2. Aim of the work

Although several empirical and numerical models exist for porous screens, two major gaps remain: (i) the absence of a general and experimentally feasible methodology for aerodynamic characterisation and (ii) the lack of a systematic comparison between the three main techniques used to estimate aerodynamic forces:

1. Balance-based force measurements (Shen et al., 2025);
2. total-pressure drop across the screen (Allori et al., 2013);
3. static-pressure difference across the plate (Pomaranzi et al., 2021a).

These methods are often treated as equivalent, despite relying on different physical assumptions and measurement locations.

This work addresses the aforementioned gaps through a hybrid CFD–WT approach. High-resolution numerical simulations guide the design of an "optimised" experimental setup to enable rapid characterisation of porous geometries. Wind-tunnel tests are then used to quantify the consistency and limitations of the three force-estimation techniques and to validate the simplified CFD setup based on a cyclic "modulus" configuration, where only the smallest repeating unit of the perforated plate is simulated.

The combined numerical–experimental strategy presented in this study aims to provide a robust and transferable framework for the aerodynamic characterisation of porous elements, with direct implications for façade engineering and wind–structure interaction problems.

The adopted methodology is presented in Section 2. The experimental and numerical setups are described in Sections 3 and 4, respectively. The results are reported and discussed in Section 5, and the main findings are summarised in Section 6.

2. Methodology

The aerodynamic characterisation of perforated plates requires a repeatable approach combining experimental measurements and numerical modelling. This study focuses on thin perforated sheets, where the aerodynamic response is primarily governed by drag. Previous research (Allori et al., 2013; Marykovskiy et al., 2024) indicates that the lift component is at least an order of magnitude smaller than drag, due to limited thickness and weak flow deviation. Consequently, the methodology focuses on the determination of the drag coefficient, although the framework remains applicable to three-dimensional porous media, such as expanded meshes or louvers.

Three reference plates with porosities $\beta = 65.8\%$, 46.5%, and 40.3% are analysed both numerically and experimentally. A validated CFD environment is then used to test numerically seven additional variants, differing in hole scale, shape, and alignment, to investigate aerodynamic behaviour as a function of porosity, pattern, and wind angle.

A central element of this work is the comparison of three approaches used to estimate the aerodynamic force acting on a porous screen. Under a constant flow rate, these quantities describe the same global drag phenomenon, yet they include different physical contributions:

1. **Force-based method.** The normal force is obtained via a force balance or by integrating surface pressure and shear stress in CFD. The coefficient is defined as:

$$C_{n,B} = \frac{F_n}{0.5\,\rho\,U^2\,A}, \tag{9}$$

where F_n is the normal force and A is the gross frontal area. This method serves as the reference for the aerodynamic load, as it directly captures the fluid–structure interaction (Shen et al., 2025).

2. **Total-pressure-drop method.** This formulation relates the aerodynamic force to the total-pressure deficit $\Delta p_{MV} = p_{t,M} - p_{t,V}$ measured upstream and downstream of the plate (Allori et al., 2013):

$$C_{n,MV} = K = \frac{\Delta p_{MV}}{0.5\,\rho\,U^2}. \tag{10}$$

Physically, this value includes all losses within the setup, such as boundary wall friction and three-dimensional flow effects.

3. **Static-pressure method.** The static pressure difference $\Delta p_G = p_{s,U} - p_{s,D}$ is measured locally on the two faces of the plate:

$$C_{n,G} = \frac{\Delta p_G (1-\beta)}{0.5\,\rho\,U^2}. \tag{11}$$

The term $(1-\beta)$ accounts for the solid portion of the reference area on which the static pressure acts: $A_s = A(1-\beta)$.
This method is common in complex wind tunnel setups, such as façade tests (Pomaranzi et al., 2019, 2021a), but it only captures pressure-driven forces and is sensitive to the local tap position.

Experimental tests are conducted in a closed-loop wind tunnel at a controlled mass flow rate. The plates are mounted on a rotatable support to adjust the angle of attack while minimising interference. Force, total pressure, and static pressure are acquired simultaneously to ensure a direct comparison under identical conditions.

To support the experimental data, CFD simulations are performed at three levels of complexity. First, explicit simulations of the wind tunnel evaluate the influence of supports and sensor placement. Second, the full test section is modelled to quantify flow uniformity and boundary effects. Third, a simplified "modulus" configuration models only the smallest repeating unit of the plate using cyclic boundary conditions. This periodic domain removes wall effects and allows for high spatial resolution at a reduced computational cost.

The modulus configuration is validated against experimental results and full-scale simulations by comparing force-based drag measurements ($C_{n,B}$). It is then used to evaluate the influence of porosity, pattern, and incidence angle, and to derive a correction factor for the static-pressure method that accounts for the non-uniformity of the surface pressure field. This combined strategy provides a general methodology for the characterisation of porous elements. Although developed for thin perforated plates, the approach can be extended to more complex porous structures, including expanded meshes and louvers, where anisotropy and directional permeability require an accurate characterisation.

3. Experimental setup

The experimental campaign was conducted in the high-speed section of the Politecnico di Milano wind tunnel model, a 1:9 closed-circuit replica of the full-scale facility (Fig. 1(a)). The high-speed test section consists of a square duct equipped with an upstream convergent and a downstream divergent, providing stable and repeatable inflow conditions (smooth-flow, $I_u < 1\%$) under an imposed flow-rate operation. The dimensions of the test section are 0.45 m × 0.45 m × 0.45 m.

Three perforated plates were tested, labelled Q, R and T, with porosities of $\beta = 65.8\%$, 46.5% and 40.3%, respectively. Their geometries at normal wind incidence are shown in Fig. 2, their thickness is $t = 2$ mm.

For each plate, four wind-attack angles were investigated: $\alpha = 0°$, 15°, 30°, and 45°. The plate always spans the full width of the test chamber; therefore, for each angle, the in-plane length of the plate is adjusted so that its projected width matches the cross-section of the tunnel. Thus, given A_0, the reference area for the zero angle of attack (i.e. the frontal area of the considered plate), at the wind angle α, the total reference area is:

$$A = \frac{A_0}{\cos(\alpha)}.$$

Each plate–angle combination (e.g., R30 for plate R at $\alpha = 30°$) was tested twice at three flow velocities to verify the repeatability of results and the Reynolds independence.

The plates are mounted on a stiff steel support connected to a six-axis balance located below the test section. The support ensures minimal deformation during operation and prevents contact with the tunnel walls for all tested angles. Its aerodynamic influence was quantified through dedicated CFD simulations and confirmed experimentally: forces generated by the support alone are approximately one order of magnitude smaller than those measured with a perforated plate installed. A small ramp was placed upstream at the lower edge of the plate to reduce local separation induced by the support (Fig. 1(b)).

Aerodynamic forces are measured using the six-axis balance, which provides the full force and moment vector. Only the in-plane forces (F_x, F_y) are used to derive the normal and tangential aerodynamic coefficients, according to Eqs. (1) and (2). The x axis of the balance is directed parallel to the wind direction, therefore drag F_n and lift F_t have the following expression.

$$\begin{cases} F_n = F_x cos(\alpha) + F_y sin(\alpha) \\ F_t = F_x sin(\alpha) - F_y cos(\alpha) \end{cases} \tag{12}$$

The balance's resolution is approximately 0.1 N. Cross-talk between in-plane force components remained below 1–2.5%, which is acceptable given the expected load range. The balance output is sampled using a National Instruments acquisition system.

Both total and static pressure measurements complement the force data. Two Pitot tubes are installed: one upstream ($p_{t,M}$), at the end of the convergent, and one downstream ($p_{t,V}$), at the beginning of the divergent, as clarified by Fig. 1(c). These measures are used to estimate the total pressure drop Δp_{MV} in Eq. (10). Their positions are close to the centre of the cross-section to minimise wall-induced bias. Each Pitot is connected to a Furness micromanometer, providing the instantaneous dynamic pressure used to estimate the reference wind speed (U).

A cross-calibration was performed by placing both Pitot–Furness pairs side by side at different tunnel speeds. The systematic difference between the two dynamic-pressure readings was approximately 2 Pa, a value adopted as the uncertainty on total-pressure measurements.

Static pressures on the perforated plates are acquired with a multi-channel pressure scanner with a resolution of 0.5 Pa. Each plate is instrumented with six static taps: three on the upstream face ($p_{s,U1-3}$) and three on the downstream face ($p_{s,D1-3}$) (see the examples reported in Fig. 3(a)). These measures are used to estimate the static pressure drop across the grid Δp_G in Eq. (11). They are ordered from the geometric centre to the lateral edge, providing a minimal representation of the streamwise pressure distribution across the plate. For the plate with the lowest porosity (T), drilling between holes is not feasible, therefore custom flush-mounted adapters were used to fix the pressure taps (Figs. 3(c) and 3(d)).

All signals (forces, dynamic pressures, static pressures) are acquired synchronously. For each configuration, two time series of 30 s are recorded for each velocity in steady-state conditions to assess repeatability.

4. Numerical setup

All numerical simulations were performed using OpenFOAM-12, solving the incompressible steady-state Reynolds-averaged Navier–Stokes (RANS) equations with the k–ω SST turbulence model. Steady-state RANS was preferred over transient simulations (DES/LES) to maintain computational efficiency across the multi-scale domain hierarchy, from the full wind tunnel to the periodic modulus. Since the study focuses on the estimation of time-averaged aerodynamic loads, the RANS approach represents the standard and most practical choice in accordance with established porous media literature (Tominaga and Shirzadi, 2022; Raffaele and Coste, 2025). The numerical setup described in this section applies consistently across all geometries and inflow conditions.

The solver employed is `foamRun`, with standard SIMPLE pressure–velocity coupling. Convective terms are discretised using second-order upwind schemes, while diffusive terms adopt central differencing. Gradients are linearly interpolated, and turbulence quantities rely on wall functions for k, ω and turbulent viscosity ν_t. Adaptive low-Re wall functions employed in OpenFOAM (e.g., *kqRWallFunction* and *omegaWallFunction*) were selected to ensure physical consistency at all y^+ values (Liu, 2016). Convergence is enforced by monitoring both residual

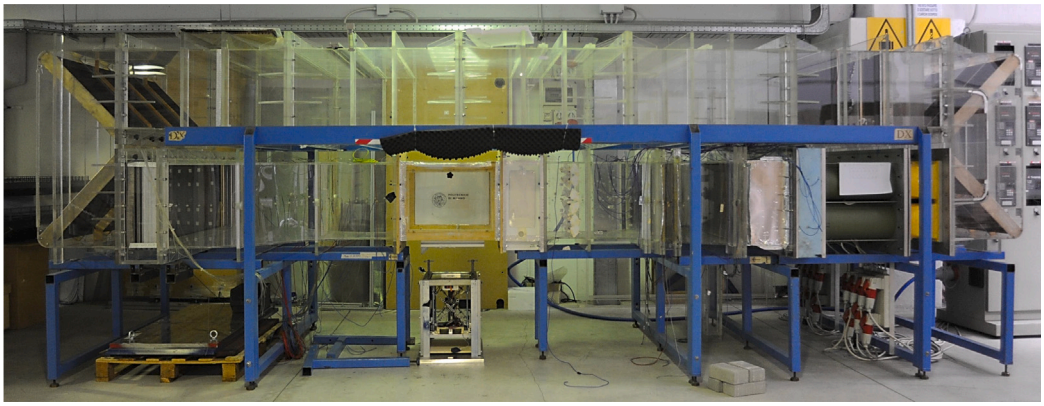

(a) Wind tunnel.

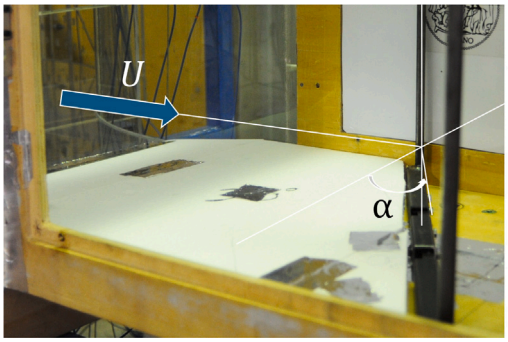

(b) Zoom of the test section.

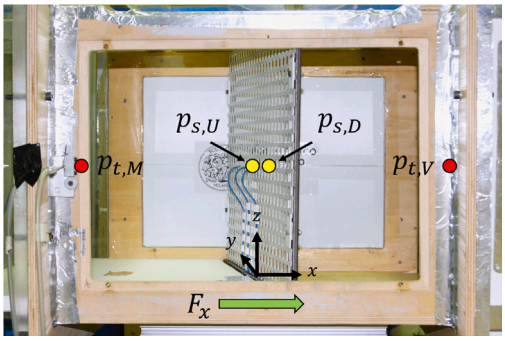

(c) Sketch of the measured quantities.

Fig. 1. Experimental setup.

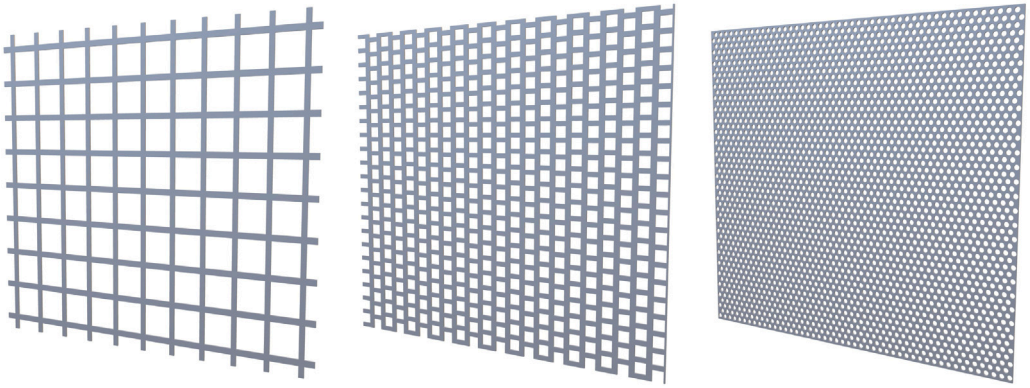

(a) Q – $\beta = 65.8\%$ (b) R – $\beta = 46.5\%$ (c) T – $\beta = 40.3\%$

Fig. 2. CAD model of the three tested plates.

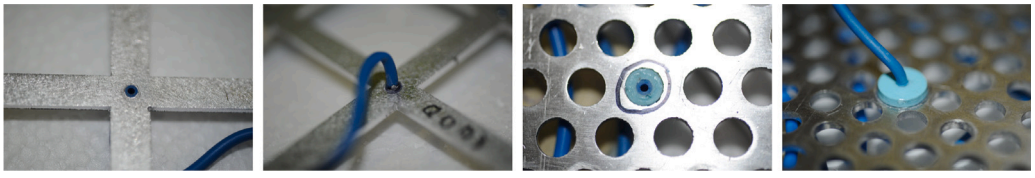

(a) Q, upwind tap. (b) Q, downwind tap. (c) T, upwind tap. (d) T, downwind tap.

Fig. 3. Zoom on the static pressure taps on Q and *T* plates.

Table 2
Mesh properties of the ten modulus simulations.

Geometry	Number cells [M]	$\frac{D_H}{l}$	$\frac{s}{l}$	Max y+
Q	3.51	236	60	5.06
Q-s	1.06	118	30	5.09
Q-c	0.376	61	11	3.38
R	2.40	106	46	5.93
R-a	2.43	106	53	5.98
R-ac	2.43	120	38	4.82
R-s	0.856	53	23	5.56
T	0.436	48	24	4.85
T-a	0.376	68	26	5.74
T-aq	0.421	60	34	7.63

decay, below 10^{-6} for momentum and 10^{-7} for turbulence variables, and the stability of the integral forces on the plate.

Three types of numerical domains are considered. Firstly, the full wind tunnel geometry reproduces the convergent, test section, and the initial part of the divergent used during experiments, including an explicitly modelled perforated plate and support. This configuration is used to simulate the global flow and to evaluate the uniformity of the velocity field in the test section.

A more refined simulation, the so-called "quarter wind tunnel", reproduces just a quarter of the domain, exploiting its symmetry, and allowing for higher mesh resolution and accuracy. The perforated element is modelled alone, without the experimental support. In this second configuration, the analysis focuses on the inner portion of the grid, measuring aerodynamic quantities in the undisturbed region.

Thirdly, the "modulus" domain represents the elementary periodic unit cell of the perforated element. By applying cyclic boundary conditions to all lateral faces, the model simulates an infinitely periodic plate, effectively isolating the intrinsic aerodynamic properties of the medium from edge- or frame-induced disturbances. In this framework, the domain geometry remains invariant across all simulated cases, making it particularly suitable for parametric studies. Simulations at non-zero angles of attack are achieved solely by modifying the inlet boundary condition, where the velocity vector is prescribed in terms of its projected components.

Although this approach ensures geometric consistency, high angles of incidence ($\alpha > 60°$) result in a reduced numerical convergence rate, due to the increased complexity of mapping skewed flow structures across the cyclic boundaries. Nevertheless, numerical stability and accuracy remain unaffected provided that convergence is monitored through the steady-state behaviour of integral quantities—such as force coefficients and pressure drop—in addition to standard residual decay.

All meshes are generated with `blockMesh` and `snappyHexMesh`, following a consistent refinement strategy. Coarser background regions are combined with progressively refined boxes around the plate and within the flow channels. In the full wind tunnel model, meshes typically contain 9 – 15 million cells, depending on the specific geometry and inflow condition (Fig. 4(a)). The quarter wind tunnel configuration employs a smaller but more refined domain, with approximately 4 – 6 million cells, allowing better resolution of the jetting and recirculation downstream of the element (Fig. 4(b)). The modulus meshes reach 3 – 4 million cells, with a minimum cell size l of approximately 0.125 mm near the perforation edges (Fig. 4(c)). This small element size grants an adequate resolution of the solid ligaments and holes (see Table 2 $\frac{s}{l}$ and $\frac{D_H}{l}$ metrics respectively) and a maximum y^+ lower than 8 for all the tested geometries.

A mesh-independence analysis was performed by repeating selected simulations on systematically refined grids to ensure numerical convergence across all domain types. Table 3 presents the drag coefficients $C_{n,B}$ for the Q-series geometries in the modulus configuration as a representative case. Three mesh resolutions, coarse, standard, and fine, were compared. The aerodynamic loads showed negligible variations (below 1%) between the standard and fine refinements, indicating that the adopted resolution is sufficient to provide mesh-independent results for all investigated geometries.

Table 3
Comparison of the drag coefficient $C_{n,B}$ for the adopted mesh, a coarser and a finer version, modulus configuration. Only the highest wind speed (10 m/s) is reported.

Geometry	$C_{n,B}$ [-]			Number cells [M]		
	Coarse	Adopted	Fine	Coarse	Adopted	Fine
Q	1.50	1.50	1.50	0.415	3.51	8.25
Q-s	1.46	1.47	1.46	0.166	1.06	7.86
Q-c	1.40	1.47	1.46	0.0780	0.376	3.03

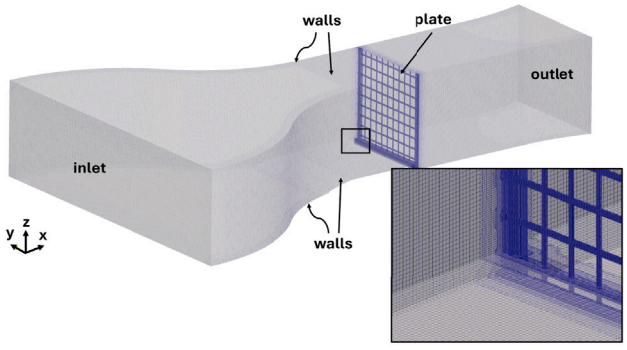

(a) Full wind tunnel mesh.

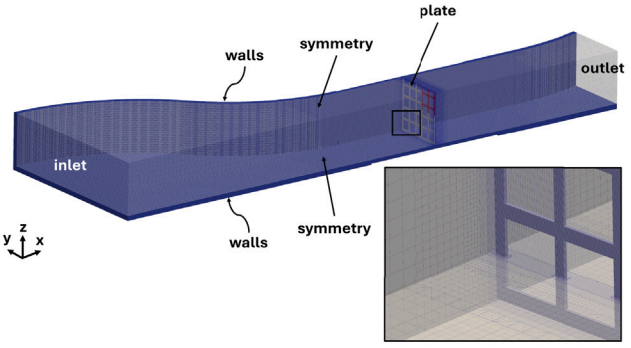

(b) Quarter wind tunnel mesh.

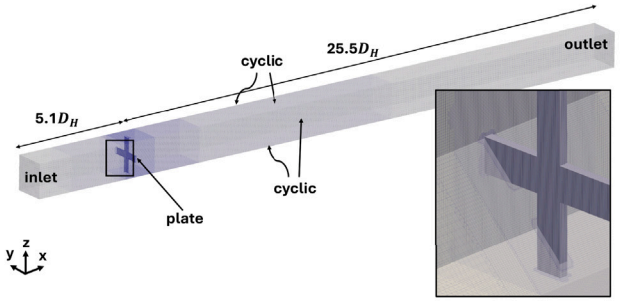

(c) Modulus configuration mesh.

Fig. 4. Meshes and computational domain employed along with a zoom to highlight refinement near the walls.

Boundary conditions are applied consistently across all simulations. In the full wind-tunnel domain, a fixed uniform velocity is imposed at the inlet, a fixed static pressure at the outlet, and no-slip conditions are used on the walls and on the perforated plate. Symmetry planes are used when allowed by the geometry. In cyclic domains, the flow enters with a fixed velocity and exits through a zero-pressure outlet; all lateral faces are cyclic, while the plate surfaces are treated as no-slip

Table 4
Boundary conditions for the full wind-tunnel domain.

Field	Inlet	Outlet	Walls/Plate	Symmetry[a]
p	zeroGradient	fixedValue (0)	zeroGradient	symmetry
U	fixedValue (U)	inletOutlet	noSlip	symmetry
ν_t	calculated	calculated	nutkWallFunction	symmetry
k	fixedValue	inletOutlet	kqRWallFunction	symmetry
ω	inletOutlet	inletOutlet	omegaWallFunction	symmetry

[a] When present, see for example the mesh in Fig. 4(b).

Table 5
Boundary conditions for cyclic domains.

Field	Inlet	Outlet	Cyclic	Plate
p	zeroGradient	fixedValue (0)	cyclic	zeroGradient
U	fixedValue (U)	inletOutlet	cyclic	noSlip
ν_t	calculated	calculated	cyclic	nutkWallFunction
k	fixedValue	inletOutlet	cyclic	kqRWallFunction
ω	inletOutlet	inletOutlet	cyclic	omegaWallFunction

walls with appropriate wall functions. The main boundary conditions are summarised in Tables 4 and 5.

4.1. Tested geometries

The three perforated plates tested experimentally (Q, R, T reported in Fig. 2) are all simulated numerically in the three domains described above. In addition, seven variants of these geometries are considered to explore the influence of the hole pattern. These modified moduli, labelled *A-xx*, share the same porosity level A (Q, R or T), while *xx* specifies the type of modification: *s* for uniformly in-plane downscaled features by 0.5, *c* and *q* for circular or rectangular perforations respectively, and *a* identifies hole alignment along the y and z directions. As an example, configurations R-a and R-ac are both characterised by porosity $\beta = 46.5\%$ (as the reference R) and aligned holes, but the first has square perforations, and the latter round perforations. All moduli have a constant thickness of 2 mm, consistent with the experimental plates.

These seven additional geometries are simulated in the modulus configuration at normal incidence (see Fig. 5). In the cyclic domains, each plate is tested at four streamwise velocities: 10, 7.5, 5 and 2.5 m/s; while for the "full-WT" simulations, velocities corresponding to those measured in the wind-tunnel tests are chosen.

For the analysis of skew inflow at angles of attack $\alpha = 0°$, 15°, 30°, 45°, the inlet velocity components are prescribed as

$$U_x = U\cos\alpha, \qquad U_y = U\sin\alpha,$$

where the secondary direction corresponds to the in-plane periodic direction of the modulus. For all simulations, the integrated forces on the perforated surface, the local pressure distributions, the pressure drop across the element and the velocity field in the vicinity of the perforations are extracted. These quantities form the basis for the comparison between the different numerical configurations and with the experimental measurements presented subsequently. In the following section, results are discussed using $C_{n,B}$ as the main aerodynamic load descriptor.

A summary of the tested configuration is reported in Table 6.

5. Results

5.1. Validation of the modulus approach

As a first step, the incoming flow field was analysed for the reference configuration with the plate normal to the wind direction ($\alpha = 0°$). The mean velocity profiles were sampled at several along-wind positions, from $x/D_H = -8.1$ (upstream) to $x/D_H = 8.1$ (downstream), where the origin of the reference system corresponds to the upwind grid plane.

Fig. 6(a) reports vertical (z-direction) and horizontal (y-direction) velocity profiles for configuration Q0. The incoming flow exhibits an acceleration up to approximately $U = 1.1U_{ref}$ near the lateral boundaries ($y/D_H > 6$), likely induced by the convergent section. This non-uniform inflow produces a higher local pressure coefficient C_p on the external portion of the plate (Fig. 6(b)), leading to a systematic overestimation of the drag coefficient when forces are integrated over the entire grid.

For this reason, only the central region of the plate, where the incoming velocity profile is essentially flat, was used as the reference for validating the modulus configuration. By extracting forces and pressures only from this portion, wall-induced flow non-uniformities are removed.

Table 7 compares the drag coefficients computed using the three definitions in Eqs. (9), (10), and (11) for the full plate, the isolated central region, and the modulus configuration. Results are reported for Q0 at $U_{ref} = 10.6$ m/s, although similar trends are observed for all other porosities and wind speeds, ensuring that the $Re_H > 3000$ criterion is respected (Allori et al., 2013).

The comparison between the full-plate and central-region values of $C_{n,B}$ shows a discrepancy of approximately 6.6%, which can be interpreted as the magnitude of the wall-induced bias affecting the full WT simulation.

The coefficient $C_{n,MV}$ yields values approximately 2.5% larger than the reference. This behaviour is consistent with the physics underlying the total pressure drop: the measured Δp_{MV} includes both (i) the local loss across the perforated plate and (ii) the distributed losses due to wall friction along the WT. In the modulus configuration, where no walls are included, this bias disappears entirely, and the difference between $C_{n,B}$ and $C_{n,MV}$ falls below the numerical error.

In contrast, $C_{n,G}$ systematically overestimates the drag coefficient. This error stems from the pointwise nature of the static pressure measurement, which implicitly supposes a uniform pressure field on the upstream face of the plate. This assumption is not valid because the pressure distribution is not spatially uniform. Consequently, this discrepancy persists even when using the modulus configuration. A more detailed analysis of this effect is presented in the following subsection.

Overall, the agreement between the three force-estimation methods, together with the comparison against the full WT simulation, confirms that the modulus configuration reproduces the aerodynamic behaviour of the perforated plate with high physical fidelity and a fraction of the computational cost. All parametric analyses presented hereafter therefore rely on modulus simulations, except where explicitly stated differently.

5.2. Static-pressure correction: γ

Estimating the drag from the static-pressure difference across the perforated plate is attractive because it requires minimal instrumentation and remains applicable even when the use of a balance or Pitot tubes is impractical. However, this method implicitly assumes that the static pressure is spatially uniform on both faces of the plate, such that two pointwise measurements capture the surface-averaged pressure field: CFD results clearly demonstrate that this assumption is not valid. On the windward face, the pressure coefficient displays a strongly heterogeneous pattern: stagnation occurs only at the centres of the solid ligaments, whereas regions of markedly lower pressure appear near the hole edges due to local acceleration and streamline curvature (Fig. 7(a)). Although the leeward face exhibits a more homogeneous distribution, it still departs from the idealised uniform field assumed by the pointwise approach. Fig. 7(b) shows the upwind and downwind distributions of C_p along the local coordinate s for the Q0 modulus, highlighting the difference between pointwise measurements and the

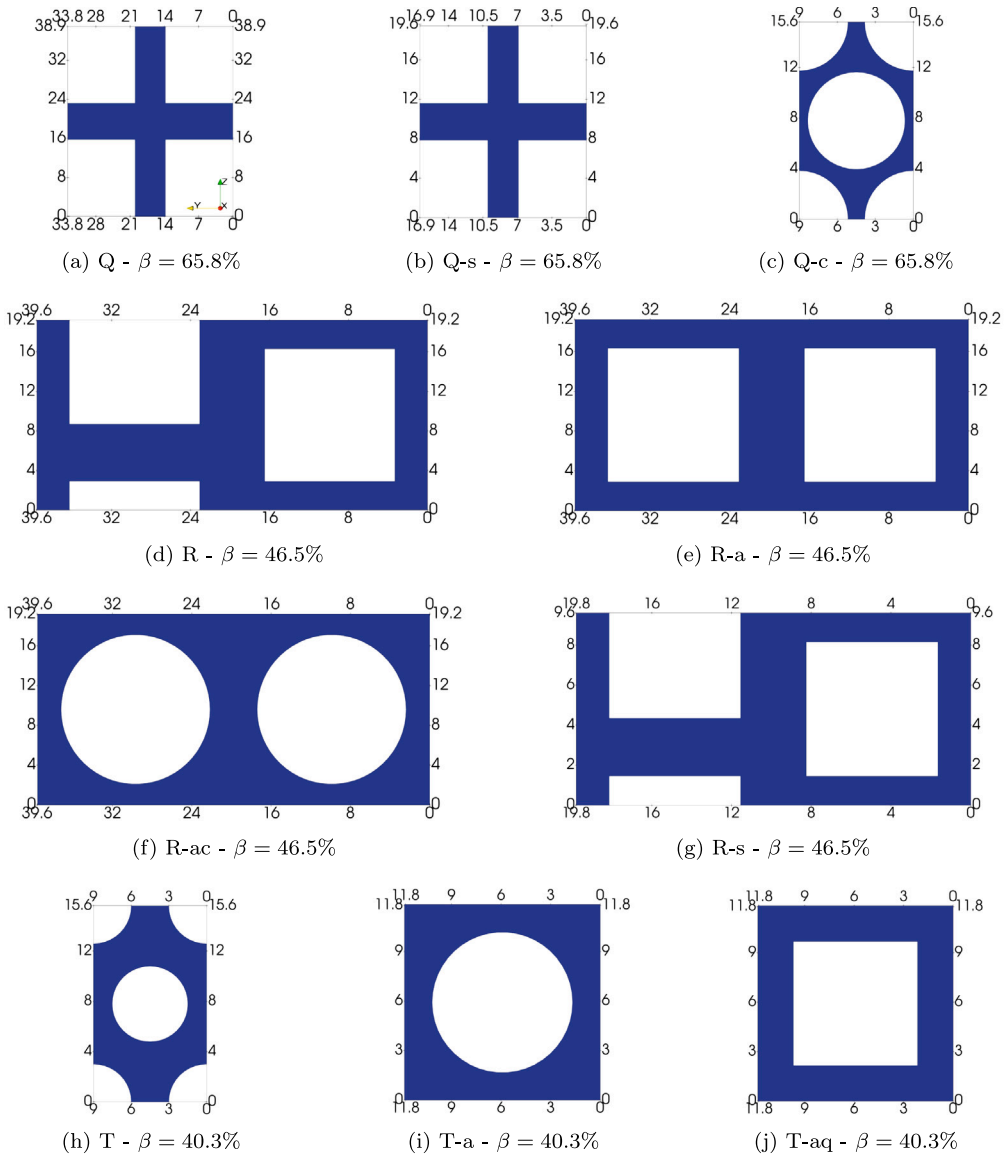

(a) Q - $\beta = 65.8\%$ (b) Q-s - $\beta = 65.8\%$ (c) Q-c - $\beta = 65.8\%$

(d) R - $\beta = 46.5\%$ (e) R-a - $\beta = 46.5\%$

(f) R-ac - $\beta = 46.5\%$ (g) R-s - $\beta = 46.5\%$

(h) T - $\beta = 40.3\%$ (i) T-a - $\beta = 40.3\%$ (j) T-aq - $\beta = 40.3\%$

Fig. 5. Geometries of the ten considered moduli simulated in cyclic conditions. Dimensions in millimetres.

Table 6
Summary of the experimental and numerical test matrix.

Geometries	Experimental	Full/Quarter WT	Modulus CFD	Angles (α)
Reference (Q, R, T)	✓	✓	✓	0°, 15°, 30°, 45°
Parametric Variants (Fig. 5)	×	×	✓	0°

Table 7
Comparison C_n obtained with the three methods for the three CFD configurations: full WT, central grid and modulus, Q0 configuration.

Configuration	$C_{n,B}$	$C_{n,MV}$	$C_{n,G}$
Full WT (entire plate)	1.29	1.24	1.34
Central region	1.21	1.24	1.34
Modulus	1.19	1.19	1.23

true spatial mean. As a consequence, the measured static-pressure jump $\Delta p_G = p_{s,U} - p_{s,D}$ does not correspond to the surface-integrated pressure force, leading to a systematic overestimation of the drag coefficient $C_{n,G}$ relative to the force-based reference value $C_{n,B}$.

To correct this intrinsic bias, the pressure field should be represented by an averaged contribution over the entire surface. For this purpose, the pressure-correction factor γ is introduced:

$$\gamma = \frac{C_{n,G}}{C_{n,B}} - 1 \quad [\%]. \tag{13}$$

The coefficient γ represents the percentage deviation of the pointwise static-pressure estimate ($C_{n,G}$) from the true aerodynamic load ($C_{n,B}$), the latter being derived from the full surface integration of pressure and shear stresses. It serves as the correction required to align local measurements taken at the ligament centre with the spatial average across the plate.

A positive value ($\gamma > 0$) indicates that the sampled local pressure exceeds the surface mean. This is the expected physical scenario, as the pressure distribution reaches its peak at the ligament centre, which corresponds to the stagnation point. A negative correction factor is physically improbable, as it would imply a surface-averaged pressure

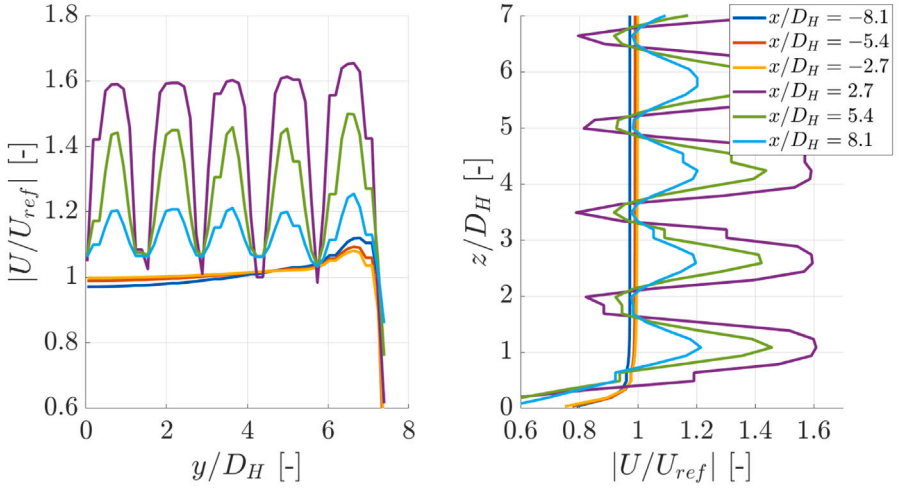

(a) Wind speed profile. Left: U/U_{ref} along y at $z/D_H = 4.6$. Right: U/U_{ref} along z at $y/D_H = 0.54$.

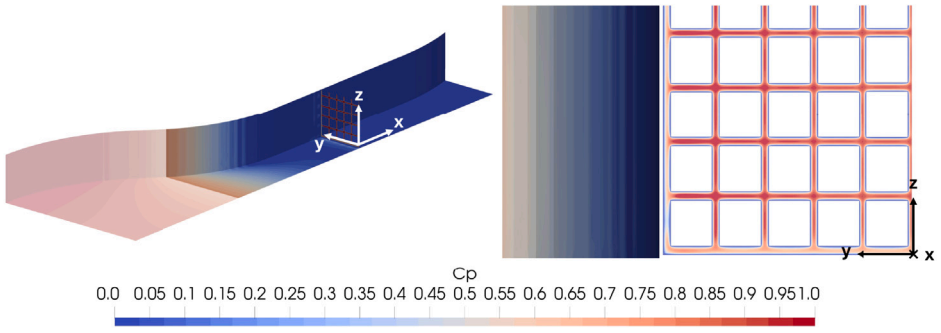

(b) Distribution of the pressure coefficient C_p mapped on the internal walls of the wind tunnel convergent section and on the upstream face of the grid.

Fig. 6. Velocity and pressure fields from quarter wind tunnel simulation, configuration Q0.

higher than the local stagnation peak. Consequently, the coefficient compensates for the inherent non-uniformity of the pressure field, providing a physically consistent estimate of the load-driving pressure jump from local tap data.

The resulting values of γ for all geometries are compared in Fig. 8, where the correction coefficient is plotted against the non-dimensional spacing D_H/s. This quantity includes information on both the dimension and shape of the hole (through the hydraulic diameter D_H) and the extension of the bulk section (through the ligament spacing s). As can be observed from the plot, two configurations with different porosity might share the same non-dimensional spacing (see configurations T and R-a), while two configurations with the same porosity have the same D_H/s only if they are characterised by the same hole shape (see configurations Q and Q-s). This highlights the capability of the introduced parameter to capture not only empty and total space ratio (as the porosity coefficient β), but also how the solid space is distributed, introducing the effect of hole shape and geometry.

A low value of D_H/s represents a geometry with small or well-spaced holes, while a high value of D_H/s indicates that the modulus area is dominated by holes close to each other. It can be observed that for $1.5 < D_H/s < 5$, γ falls within a narrow range of 4%–6%. At higher non-dimensional spacing, specifically $D_H/s = 5.7$ for the Q-c geometry, a $\gamma = 10\%$ would be required. This behaviour is consistent with its minimal ligament spacing, which is the cause of a sharp C_p distribution and thus a higher correction coefficient. Considering the compact distribution of the remaining data, a representative and broadly applicable correction factor of $\gamma \approx 5\%$ can be adopted for the geometries $1.5 < D_H/s < 5$.

For $D_H/s < 1.5$ scenarios, the pressure field is expected to be significantly flatter. In this limit, the stagnation pressure at the ligament centre becomes representative of the surface mean, causing γ to approach zero. For $D_H/s > 5$ the approach remains valid, but ad-hoc modulus simulations should be performed to derive the correct value of γ.

It must be acknowledged that since the surface pressure field is inherently non-uniform, any pointwise measurement is configuration-dependent. Therefore, the proposed sampling at the ligament centre should be regarded as a practical, physically motivated convention rather than a universally representative measurement. By targeting the stagnation region, this strategy captures the peak positive pressure, representing a conservative convention for load estimation. While any other sampling location would result in a different correction factor, this specific placement ensures repeatability across different geometries.

5.3. Influence of porosity and hole pattern

Fig. 9 reports the evolution of the total pressure coefficient along the streamwise direction for $\alpha = 0°$, sampled along a line crossing the centre of the bulk region of each modulus. All geometries display a peak at $C_p = 1$ at the stagnation point, confirming that the sampling line intersects the region of maximum flow impingement. Immediately downstream of the stagnation location, a sharp discontinuity appears.

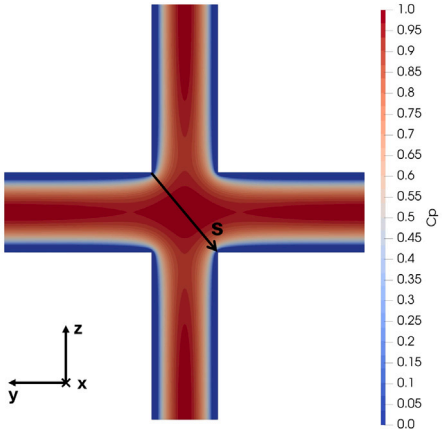

(a) C_p distribution on the upwind face of the modulus.

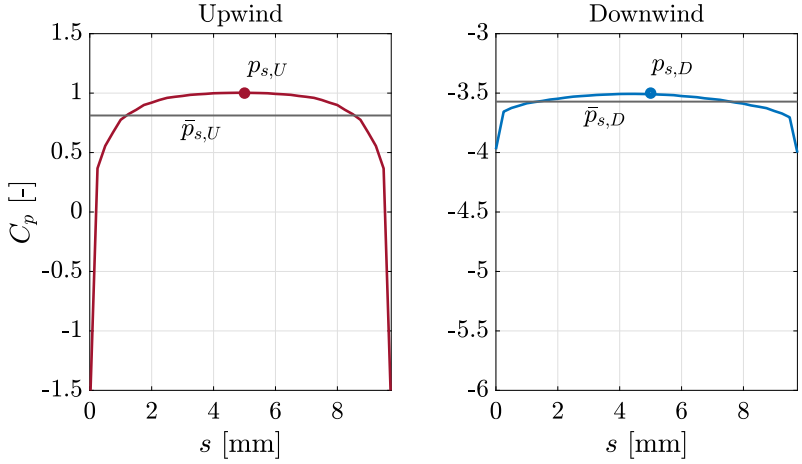

(b) Upwind and downwind distribution of C_p along the coordinate s. The markers indicate the pointwise measurements ($p_{s,U}$ and $p_{s,D}$) used for evaluating $C_{n,G}$, while the grey lines denote the spatial averages ($\bar{p}_{s,U}$ and $\bar{p}_{s,D}$) along the same path.

Fig. 7. Pressure coefficient distribution for the Q0 modulus.

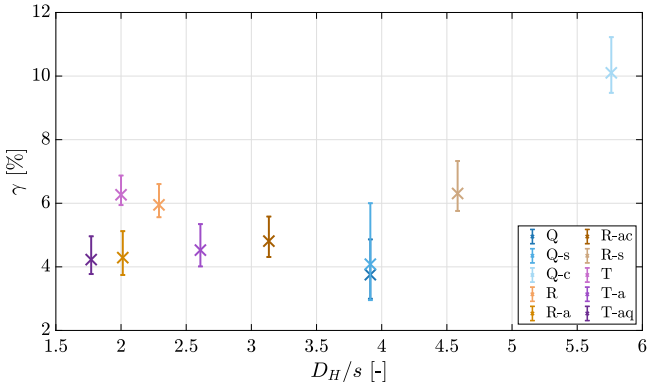

Fig. 8. Pressure correction coefficient γ for all tested geometries, plotted against the non-dimensional spacing D_H/s. Each geometry is colour-coded by porosity: blue ($\beta = 65.8\%$), yellow ($\beta = 46.5\%$), and purple ($\beta = 40.3\%$). Error bars reflect measurements repeated at different wind speeds.

This jump corresponds to the static-pressure drop imposed by the porous medium. A pronounced minimum follows within $0 < x/D_H < 1$, marking the core of the wake, after which a gradual and monotonic recovery occurs. For all tested geometries, the pressure field reaches its asymptotic value at approximately $x/D_H \approx 8$, indicating that the extent of the near-wake region is largely insensitive to the specific hole pattern and depends primarily on the global blockage effect of the grid.

Analysis of the full dataset confirms a clear and monotonic relationship between porosity and drag coefficient: decreasing porosity leads to a nonlinear increase in C_n. This behaviour is reflected in the pressure field, where low-porosity configurations exhibit larger stagnation regions and stronger blockage, consistent with the classical response of porous media under normal flow.

Porosity emerges as the dominant geometric parameter. Despite some differences in the local flow structures, pressure distributions and jetting patterns among the various hole arrangements, the global force coefficients vary only slightly at fixed porosity, typically within 2%–4%. This indicates that the hole pattern primarily influences small-scale flow features, whereas the integral aerodynamic response is governed overwhelmingly by the open-area ratio.

This finding is noteworthy because it supports the use of porosity-based correction frameworks when detailed geometric information on the perforation pattern is unavailable. It also suggests that, for design-oriented or reduced-order modelling purposes, porosity alone may suffice to classify the aerodynamic behaviour of perforated panels under normal incidence.

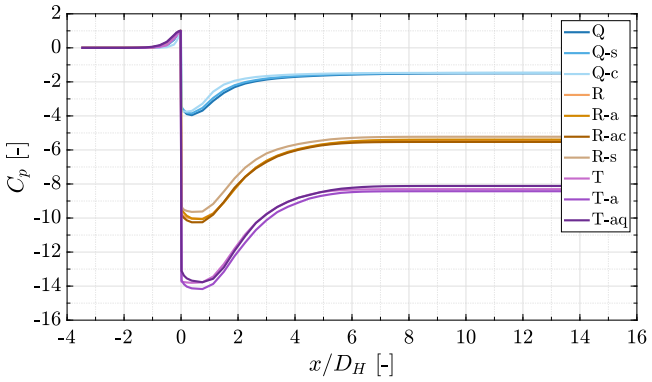

Fig. 9. Modulus configuration, $\alpha = 0°$. Total pressure coefficient C_p as a function of the normalised streamwise distance x/D_H for all tested geometries; sampling along the central bulk line.

5.4. Comparison with experimental data

The results of the wind-tunnel campaign are reported in Fig. 10, where panels (a), (b), and (c) correspond respectively to configurations Q0, R0 and T0. For each case, the three force-estimation methods are compared: the force-balance coefficient $C_{n,B}$ (Eq. (9)), the total-pressure-drop method $C_{n,MV}$ (Eq. (10)), and the static-pressure method $C_{n,G}$ (Eq. (11)). The corrected static-pressure estimate $C_{n,G\gamma}$, obtained using the pressure-correction factor γ (Eq. (14)), is also shown. Consistently with the findings from the modulus simulations, a constant value $\gamma = 5\%$ is adopted:

$$C_{n,G\gamma} = \frac{C_{n,G}}{\gamma + 1}. \tag{14}$$

In each plot, experimental measurements (blue) are shown alongside CFD results from the modulus configuration (orange) and full wind-tunnel simulations (green). For reference, experimental data from Allori et al. (2013) (purple), corresponding to comparable porosities, are included. The experimental values refer to the highest tested wind speed and include error bars derived from the uncertainty propagation of the measurement chain.

The drag coefficients obtained from the total-pressure-drop method exhibit a mild overestimation relative to the force-balance values, consistent with the behaviour observed in the CFD. However, the difference falls within the experimental uncertainty. Conversely, the static-pressure method systematically overestimates the drag, a discrepancy corrected effectively by the factor γ, which brings $C_{n,G\gamma}$ within the error bars of the other two estimators. This confirms the suitability of γ as a practical correction factor.

An exception is observed for geometry T0, where the experimental static-pressure estimator $C_{n,G}$ does not exhibit the systematic overestimation found in other cases. This deviation is attributed to the presence of the probe adapters (Figs. 3(c) and 3(d)), which locally block the perforations and effectively increase the solid-to-open area ratio at the measurement site. This geometric blockage flattens the local pressure field, causing the probed stagnation value to approach the area-averaged pressure. While this confirms the high sensitivity of local measurements to probe installation, it precludes the use of the T0 experimental static-pressure data as a pristine benchmark for validating the periodic CFD model. In this context, the modulus CFD remains the most reliable reference for characterising the undisturbed local physics of high-solidity media.

The agreement with literature is strong for the low-porosity plates (R0 and T0), whereas larger deviations occur for the most porous configuration Q0. The likely explanation is the presence of the support system shown in Fig. 3(b), which reduces the effective porosity and therefore increases the measured drag. This behaviour is reproduced

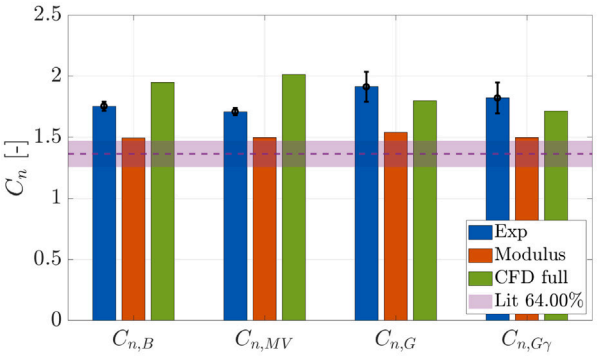

(a) Q0 configuration.

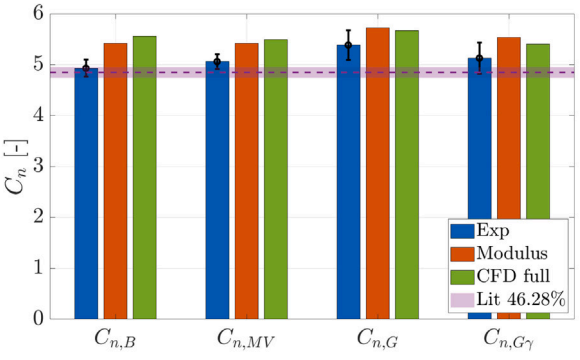

(b) R0 configuration.

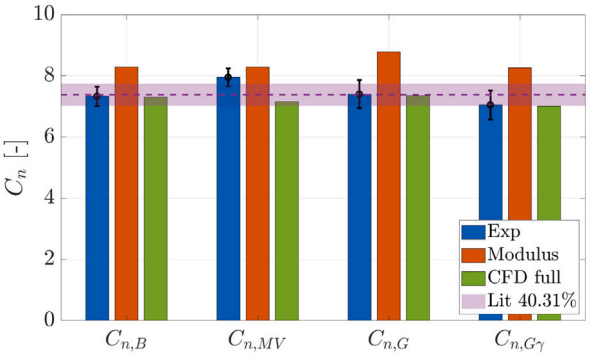

(c) T0 configuration.

Fig. 10. Drag coefficient for the three tested grid. The three force estimation methods and the correction with γ coefficient, derived from the experimental test (blue), CFD modulus configuration (orange), CFD full WT (green) and from Allori et al. (2013) (purple) are compared.

accurately in the full wind-tunnel simulations but not in the modulus simulations, which remain closer to the literature values. This further confirms that the modulus configuration captures the intrinsic fluid–structure interaction of the perforated plate without contamination from support elements or tunnel-wall effects.

The modulus CFD results show an approximate 10% overestimation compared with (Allori et al., 2013). This may be attributed to boundary-layer effects in the referenced setup, which generate a region of reduced upstream velocity near the lateral edges of the plate.

The same qualitative observations apply to the results at non-zero incidence; therefore, the full set is not plotted here and is reported instead in Appendix.

A compact representation of the dependence on the incidence angle is provided in Fig. 11, where the drag coefficients (expressed in the

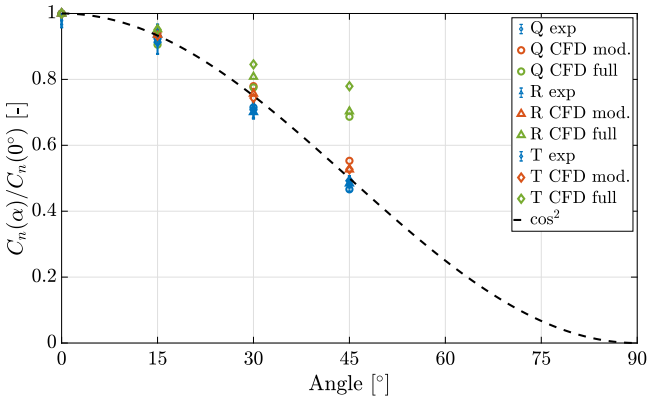

Fig. 11. Drag coefficient reduction $C_n(\alpha)/C_n(0°)$ against wind attack angle α. Comparison between experimental test (blue), CFD modulus configuration (orange), CFD full WT (green).

form of $C_{n,B}$) are normalised by their value at $\alpha = 0°$. The dashed curve represents the well-known $\cos(\alpha)^2$ trend (Eq. (8)) (Laws and Livesey, 1978; Xu et al., 2020). Markers indicate the geometry (circles for Q, triangles for R, and diamonds for T), and the colour code follows the same convention as in the previous figures: blue for the experimental results, orange for the CFD results in the modulus configuration, and green in the full-WT configuration.

Both the experiments and the modulus CFD closely follow the $\cos(\alpha)^2$ dependence, confirming that the effective projected-area mechanism governs the load variation for thin perforated plates. In contrast, the full wind-tunnel CFD produces significant overestimations and inconsistent trends, highlighting once more the difficulty of accurately simulating multiscale porous-media effects when the full experimental setup is reproduced explicitly. The modulus configuration avoids this issue and correctly captures the angle-dependent physics at a fraction of the computational cost.

Finally, it is noted that a tangential force component arises at non-zero incidence, quantified by the lift coefficient $C_{t,B}$. For thin perforated plates, this contribution is more than an order of magnitude smaller than the normal load. Given the sensitivity limits of the balance, the experimental measurements were not sufficiently accurate for validation, although the same analysis procedure could be applied to future datasets.

It should be noted that, for porous media with pronounced directional features (such as louvers) and 3D effects (such as flow deviations near the setup boundaries), which are likely more significant, the finite dimensions of a test section might cause discrepancies between experimental measurements and periodic CFD simulations. This represents a limitation of the experimental setup: the modulus configuration is specifically designed to isolate and capture the local flow-porosity interaction, providing the fundamental data required for lumped parameter models, such as the pressure-jump (Xu et al., 2020, 2023) and Darcy–Forchheimer formulations (Marykovskiy et al., 2024), when dealing with thin perforated plates.

Overall, the experimental campaign confirms the findings from the CFD analysis. The force-balance method provides the most reliable estimate of the aerodynamic load, while the total-pressure-drop method remains a viable alternative when instrumentation constraints limit force measurements. The static-pressure method systematically overestimates the drag because of the inherently non-uniform surface-pressure distribution, yet the introduction of the correction factor γ yields a consistent and physically justified adjustment that aligns the estimate with the other methods. The agreement between experiments and modulus simulations, and their coherence with established porous-plate theory, reinforces the robustness of the proposed hybrid methodology and supports the use of modulus-based CFD as the primary predictive tool in the subsequent analysis.

5.5. Practical implications for experimentalists

The comparison between numerical and experimental results provides several practical guidelines for accurate local pressure measurements on porous media. A primary concern is the sensitivity of the probe position, as the windward pressure field is highly non-uniform and configuration-dependent. The sampling strategy proposed in this work, targeting the ligament centre, should be regarded as a practical convention designed to ensure repeatability. Since this location corresponds to the stagnation region, it captures the peak positive pressure, providing a conservative basis for load estimation.

CFD simulations indicate that even millimetric shifts from this central point toward an edge lead to significant pressure drops due to flow acceleration and streamline curvature. While any other sampling location would capture a lower pressure and require a different, geometry-specific correction, the choice of the ligament centre allows for a standardised application of the $\gamma \approx 5\%$ factor within the investigated geometric range ($1.5 < D_H/s < 5$).

In configurations where measurement taps cannot be integrated directly into the plate, adapters are necessary, as seen in the T configuration (Figs. 3(c) and 3(d)). Since these adapters alter the local flow, their design should be optimised using CFD to minimise interference or to calculate specific corrections. Additionally, tubing interference can be reduced by following specific criteria: tubes must be firmly fixed to prevent flow-induced vibrations, routed exclusively along solid ligaments to avoid altering the effective porosity, and upstream/downstream lines should be separated to avoid aerodynamic interference between the due sides of the plate. Adopting these measures within a hybrid CFD–WT framework allows for a more rigorous quantification and correction of experimental errors.

6. Conclusions

This study presented a unified numerical–experimental framework for the aerodynamic characterisation of thin perforated plates, motivated by the need for reliable, transferable, and physically interpretable data for porous media used in façade engineering and similar applications. While previous works typically addressed isolated aspects of the problem, focusing either on pressure losses, forces, or on specific geometries, the present methodology integrates wind-tunnel measurements, fully resolved CFD of the experimental apparatus, and highly efficient periodic "modulus" simulations.

- A first contribution of the work is the systematic comparison of the three force-estimation approaches commonly used for porous screens: force balance, total-pressure drop, and static-pressure difference. Under imposed flow rate, these methods are often treated as equivalent, yet practical measurements reveal intrinsic biases. Experiments and CFD consistently show that the total-pressure method slightly overestimates the aerodynamic load because it includes distributed wall losses, whereas the static-pressure method systematically overpredicts the drag due to the non-uniform pressure field on the windward face. The proposed correction factor γ compensates for this effect and yields static-pressure-based estimates that align with the force-balance reference within experimental uncertainty. This is relevant for applications in which force balances cannot be used, and pressure taps represent the only feasible instrumentation.
- A second major outcome is the validation of the modulus configuration as a reliable and computationally efficient numerical model. Once benchmarked against explicit CFD and experiments, the modulus simulations reproduced the global aerodynamic coefficients of the plates with high accuracy, at a fraction of the computational cost. This enables systematic parametric studies in flow-controlled scenarios. Results show that, in the tested configurations, porosity is the dominant parameter controlling the drag,

Table A.8
Drag coefficients computed using the four methods for $\alpha = 0°$. Experimental, CFD in modulus configuration, CFD of the full WT in experimental setup and literature reference are compared. Variations are computed with respect to the experimental $C_{n,B}$ in each case.

Configuration	$C_{n,B}$		$C_{n,MV}$		$C_{n,G}$		$C_{n,G\gamma}$	
	Value	Var.	Value	Var.	Value	Var.	Value	Var.
Case Q:								
Experimental	1.75 ± 0.038	0.0%	1.71 ± 0.030	−2.6%	1.91 ± 0.12	9.0%	1.82 ± 0.13	3.8%
Modulus	1.50	−14.8%	1.50	−14.7%	1.54	−12.3%	1.50	−14.7%
Full WT	1.95	11.1%	2.01	14.8%	1.80	2.6%	1.71	−2.3%
Literature	1.36 ± 0.11	−22.3%	1.36 ± 0.11	−22.3%	1.36 ± 0.11	−22.3%	1.36 ± 0.11	−22.3%
Case R:								
Experimental	4.93 ± 0.17	0.0%	5.06 ± 0.14	2.6%	5.39 ± 0.29	9.2%	5.13 ± 0.31	4.0%
Modulus	5.42	9.9%	5.42	9.9%	5.72	16.1%	5.53	12.2%
Full WT	5.56	12.8%	5.49	11.4%	5.67	15.1%	5.40	9.6%
Literature	4.85 ± 0.11	−1.7%	4.85 ± 0.11	−1.7%	4.85 ± 0.11	−1.7%	4.85 ± 0.11	−1.7%
Case T:								
Experimental	7.33 ± 0.31	0.0%	7.95 ± 0.29	8.5%	7.40 ± 0.46	0.9%	7.05 ± 0.48	−3.9%
Modulus	8.29	13.1%	8.29	13.1%	8.79	19.9%	8.26	12.7%
Full WT	7.30	−0.4%	7.15	−2.5%	7.35	0.2%	7.00	−4.5%
Literature	7.38 ± 0.37	0.7%	7.38 ± 0.37	0.7%	7.38 ± 0.37	0.7%	7.38 ± 0.37	0.7%

Table A.9
Drag coefficients computed using the four methods for $\alpha = 15°$. Experimental, CFD in modulus configuration and CFD of the full WT in experimental setup are compared. Variations are computed with respect to the experimental $C_{n,B}$ in each case.

Configuration	$C_{n,B}$		$C_{n,MV}$		$C_{n,G}$		$C_{n,G\gamma}$	
	Value	Var. [%]	Value	Var. [%]	Value	Var. [%]	Value	Var. [%]
Case Q:								
Experimental	1.62 ± 0.033	0.0	1.61 ± 0.027	−0.86	1.66 ± 0.11	2.32	1.58 ± 0.11	−2.55
Modulus	1.41	−13.17	1.41	−13.14	1.49	−8.40	1.44	−11.48
Full WT	1.77	8.81	1.79	10.09	1.64	1.32	1.56	−3.51
Case R:								
Experimental	4.62 ± 0.15	0.0	4.76 ± 0.13	3.01	5.00 ± 0.26	8.18	4.76 ± 0.28	3.03
Modulus	5.07	9.80	5.07	9.80	5.30	14.85	5.08	10.08
Full WT	5.30	14.70	5.10	10.53	5.32	15.29	5.07	9.80
Case T:								
Experimental	6.69 ± 0.26	0.0	7.07 ± 0.24	5.62	6.20 ± 0.37	−7.45	5.90 ± 0.39	−11.86
Modulus	7.74	15.56	7.74	15.56	8.19	22.40	7.70	15.10
Full WT	6.94	3.74	6.67	−0.36	6.78	1.36	6.46	−3.47

Table A.10
Drag coefficients computed using the four methods for $\alpha = 30°$. Experimental, CFD in modulus configuration and CFD of the full WT in experimental setup are compared. Variations are computed with respect to the experimental $C_{n,B}$ in each case.

Configuration	$C_{n,B}$		$C_{n,MV}$		$C_{n,G}$		$C_{n,G\gamma}$	
	Value	Var. [%]	Value	Var. [%]	Value	Var. [%]	Value	Var. [%]
Case Q:								
Experimental	1.25 ± 0.023	0.0	1.22 ± 0.020	−3.04	1.30 ± 0.089	3.99	1.24 ± 0.094	−0.96
Modulus	1.17	−7.06	1.17	−7.06	1.29	2.76	1.24	−1.48
Full WT	1.51	20.53	1.38	9.92	1.35	7.98	1.29	2.84
Case R:								
Experimental	3.46 ± 0.098	0.0	3.74 ± 0.087	8.35	3.88 ± 0.19	12.20	3.69 ± 0.20	6.86
Modulus	4.10	18.73	4.10	18.73	4.32	25.08	4.10	18.57
Full WT	4.49	30.09	3.92	13.43	4.25	22.92	4.04	17.07
Case T:								
Experimental	5.19 ± 0.18	0.0	5.77 ± 0.17	11.18	4.98 ± 0.27	−4.04	4.74 ± 0.29	−8.61
Modulus	6.16	18.79	6.16	18.79	6.54	25.97	6.14	18.30
Full WT	6.17	18.91	5.55	7.01	5.58	7.58	5.32	2.46

Table A.11
Drag coefficients computed using the four methods for $\alpha = 45°$. Experimental, CFD in modulus configuration and CFD of the full WT in experimental setup are compared. Variations are computed with respect to the experimental $C_{n,B}$ in each case.

Configuration	$C_{n,B}$		$C_{n,MV}$		$C_{n,G}$		$C_{n,G\gamma}$	
	Value	Var. [%]	Value	Var. [%]	Value	Var. [%]	Value	Var. [%]
Case Q:								
Experimental	0.818 ± 0.012	0.0	0.932 ± 0.014	13.85	0.886 ± 0.067	8.28	0.844 ± 0.070	3.12
Modulus	0.827	1.06	0.827	1.07	0.888	8.49	0.868	6.10
Full WT	1.34	63.62	1.02	24.52				
Case R:								
Experimental	2.39 ± 0.058	0.0	2.70 ± 0.053	13.24	2.55 ± 0.13	6.75	2.43 ± 0.14	1.67
Modulus	2.85	19.59	2.84	19.19	2.88	20.64	2.71	13.74
Full WT	3.91	63.81	2.90	21.31	3.09	29.34	2.94	23.18
Case T:								
Experimental	3.61 ± 0.11	0.0	4.33 ± 0.11	19.88	3.66 ± 0.19	1.48	3.49 ± 0.20	−3.35
Modulus	4.37	21.08	4.37	21.08	4.60	27.51	4.34	20.27
Full WT	5.69	57.54	4.72	30.63	4.15	15.07	3.96	9.59

while hole pattern influences mainly local flow structures and has a limited effect on the integrated force. The wake development and pressure-recovery behaviour are also remarkably consistent across patterns when normalised by the hydraulic diameter.

The experimental campaign corroborated these findings. For all porosities, the force-based and corrected static-pressure estimates showed consistent trends, while the drag reduction with incidence angle followed the expected $\cos^2(\alpha)$ behaviour. Full wind-tunnel CFD, although valuable for interpreting wall-induced inhomogeneities, proved less suitable for quantitative predictions at oblique incidence due to the multiscale nature of the problem. In contrast, the modulus configuration remained robust across all tested conditions.

Overall, the proposed framework provides a fast, simple, and general methodology to characterise thin perforated plates. It offers practical guidance for wind-tunnel design and data interpretation, and it provides accurate reference values for numerical homogenisation strategies. In particular, the validated modulus model can directly support the calibration of advanced porous-medium formulations such as the Darcy–Forchheimer tensor, which require accurate force data for multiple angles of attack.

Future work should explore additional geometric parameters, including plate thickness and three-dimensional porosities (e.g., expanded meshes and louvers), which would broaden the applicability of the methodology and support its use in façade aerodynamics and flow-control applications.

CRediT authorship contribution statement

Marcello Catania: Writing – review & editing, Writing – original draft, Visualization, Validation, Methodology, Data curation, Conceptualization. **Filippo Giacomoni:** Writing – review & editing, Writing – original draft, Software, Methodology, Formal analysis, Data curation. **Giulia Pomaranzi:** Writing – review & editing, Writing – original draft, Supervision, Methodology, Investigation. **Paolo Schito:** Supervision, Project administration, Funding acquisition. **Alberto Zasso:** Supervision. **Claudio Somaschini:** Supervision, Project administration, Funding acquisition. **Luca Patruno:** Supervision, Project administration, Funding acquisition.

Funding

This work was partially supported by the Italian Ministry of University and Research (MUR) within the framework of the PRIN 2022 project "SaFEx" (Prot. 2022F5M4HF, CUP D53C24004030006).

Declaration of competing interest

The authors declare the following financial interests/personal relationships which may be considered as potential competing interests: Marcello Catania reports financial support was provided by Italian Ministry of University and Research (MUR). If there are other authors, they declare that they have no known competing financial interests or personal relationships that could have appeared to influence the work reported in this paper.

Appendix. Results for higher attack angles

See Tables A.8–A.11.

Data availability

Data will be made available on request.

References

Allori, D., Bartoli, G., Mannini, C., 2013. Wind tunnel tests on macro-porous structural elements: A scaling procedure. J. Wind Eng. Ind. Aerodyn. 123, 291–299. http://dx.doi.org/10.1016/j.jweia.2013.09.011.

Azizi, F., 2019. On the pressure drop of fluids through woven screen meshes. Chem. Eng. Sci. 207, 464–478. http://dx.doi.org/10.1016/j.ces.2019.06.046.

Castellano, S., Starace, G., 2025. Experimental evaluation of the loss coefficient of insect-proof agro-textiles and application to wind loads. AgriEngineering 7 (6), 168. http://dx.doi.org/10.3390/agriengineering7060168.

Catania, M., Pomaranzi, G., Fontanella, A., Zasso, A., 2024a. Modelling of wind turbines as porous disks for wind farm flow studies. J. Phys.: Conf. Ser. 2767 (5), 052049. http://dx.doi.org/10.1088/1742-6596/2767/5/052049.

Catania, M., Pomaranzi, G., Zasso, A., 2024b. The role of permeable double skin façades on the onset of VIV on high-rise buildings. J. Wind Eng. Ind. Aerodyn. 253, 105831. http://dx.doi.org/10.1016/j.jweia.2024.105831.

Catania, M., Pomaranzi, G., Zasso, A., 2026. From vortex shedding to vortex-induced vibrations: The role of porous façades. J. Fluids Struct. 143, 104538. http://dx.doi.org/10.1016/j.jfluidstructs.2026.104538, URL: https://www.sciencedirect.com/science/article/pii/S0889974626000381.

Feichtner, A., Mackay, E., Tabor, G., Thies, P.R., Johanning, L., 2021. Comparison of macro-scale porosity implementations for CFD modelling of wave interaction with thin porous structures. J. Mar. Sci. Eng. 9 (2), 150. http://dx.doi.org/10.3390/jmse9020150.

Giachetti, A., Manara, G., Bartoli, G., 2025. Permeable building envelopes: a literature review and a novel classification from the wind load perspective. J. Build. Eng. 114005. http://dx.doi.org/10.1016/j.jobe.2025.114005.

Guan, D., Zhang, Y., Zhu, T., 2003. A wind-tunnel study of windbreak drag. Agricult. Forest. Meterol. 118 (1–2), 75–84. http://dx.doi.org/10.1016/S0168-1923(03)00069-8.

Guo, B.Y., Hou, Q.F., Yu, A.B., Li, L.F., Guo, J., 2012. Numerical modelling of the gas flow through perforated plates. Process. Saf. Environ. Prot. 91 (3), 403–408. http://dx.doi.org/10.1016/j.cherd.2012.10.004.

Kemper, F., Feldmann, M., 2019. Wind load assumptions for permeable cladding elements considering the installation context. J. Wind Eng. Ind. Aerodyn. 184, 277–288.

Laws, E.M., Livesey, J.L., 1978. Flow through screens. Annu. Rev. Fluid Mech. 10 (1), 247–266. http://dx.doi.org/10.1146/annurev.fl.10.010178.001335.

Letchford, C.W., 2001. Wind loads on rectangular signboards and hoardings. J. Wind Eng. Ind. Aerodyn. 89 (2), 135–151. http://dx.doi.org/10.1016/S0167-6105(00)00068-4.

Liu, F., 2016. A thorough description of how wall functions are implemented in OpenFOAM. In: Nilsson, H. (Ed.), Proceedings of CFD with OpenSource Software. URL: http://www.tfd.chalmers.se/~hani/kurser/OS_CFD_2016.

Lo, Y.-L., Wu, Y.-T., Fu, C.-L., Yu, Y.-C., 2020. Wind load reduction effects on inner buildings by exterior porous façades. Build. Environ. 183, 107148. http://dx.doi.org/10.1016/j.buildenv.2020.107148.

Marykovskiy, Y., Pomaranzi, G., Schito, P., Zasso, A., 2024. A method to evaluate forchheimer resistance coefficients for permeable screens and air louvers modelled as a porous medium. Fluids 9 (7), 147. http://dx.doi.org/10.3390/fluids9070147.

Pomaranzi, G., Bistoni, O., Schito, P., Rosa, L., Zasso, A., 2021a. Wind effects on a permeable double skin façade, the ENI head office case study. Fluids 6 (11), 415. http://dx.doi.org/10.3390/fluids6110415.

Pomaranzi, G., Bistoni, O., Schito, P., Zasso, A., 2021b. Numerical modelling of three-dimensional screens, treated as porous media. Wind. Struct. 33, 409–422. http://dx.doi.org/10.12989/was.2021.33.5.409.

Pomaranzi, G., Daniotti, N., Schito, P., Rosa, L., Zasso, A., 2019. Experimental assessment of the effects of a porous double skin façade system on cladding loads. J. Wind Eng. Ind. Aerodyn. 196, 104019. http://dx.doi.org/10.1016/j.jweia.2019.104019.

Raffaele, L., Coste, N., 2025. CWE study of the aerodynamic interaction between a porous fence and a ground-mounted solid obstacle via pressure jump approach. J. Wind Eng. Ind. Aerodyn. 266, 106198. http://dx.doi.org/10.1016/j.jweia.2025.106198, URL: https://www.sciencedirect.com/science/article/pii/S0167610525001941.

Raju, K.G.R., Garde, R.J., Singh, S.K., Singh, N., 1988. Experimental study on characteristics of flow past porous fences. J. Wind Eng. Ind. Aerodyn. 29 (1–3), 155–163. http://dx.doi.org/10.1016/0167-6105(88)90154-7.

Richards, P.J., Robinson, M., 1999. Wind loads on porous structures. J. Wind Eng. Ind. Aerodyn. 83 (1–3), 455–465. http://dx.doi.org/10.1016/S0167-6105(99)00093-8.

Shen, G., Bao, X., Yao, J., Yu, S., 2025. Experimental investigation on wind loads of planar porous façades. J. Build. Eng. 112199. http://dx.doi.org/10.1016/j.jobe.2025.112199.

Skvorc, P., Kozmar, H., 2023. The effect of wind characteristics on tall buildings with porous double-skin façades. J. Build. Eng. 69, 106135. http://dx.doi.org/10.1016/j.jobe.2023.106135.

Tominaga, Y., Shirzadi, M., 2022. RANS CFD modeling of the flow around a thin windbreak fence with various porosities: Validation using wind tunnel measurements. J. Wind Eng. Ind. Aerodyn. 230, 105176. http://dx.doi.org/10.1016/j.jweia.2022.105176.

Xu, M., Patruno, L., Lo, Y.-L., Miranda, S.D., 2020. On the use of the pressure jump approach for the simulation of separated external flows around porous structures: A forward facing step. J. Wind Eng. Ind. Aerodyn. 207, 104377. http://dx.doi.org/10.1016/j.jweia.2020.104377.

Xu, M., Patruno, L., Miranda, S.D., 2023. A pressure–velocity jump approach for the CFD modelling of permeable surfaces. J. Wind Eng. Ind. Aerodyn. 233, 105317. http://dx.doi.org/10.1016/j.jweia.2023.105317.